

Single-Atom Alloy Catalysts Designed by First-Principles Calculations and Artificial Intelligence

Zhong-Kang Han,^{1,4} Debalaya Sarker,^{1,4} Runhai Ouyang,^{2,4} Yi Gao,^{3*} Sergey V. Levchenko^{1*}

¹ Center for Energy Science and Technology, Skolkovo Institute of Science and Technology, Skolkovo Innovation Center, Moscow, 143026, Russia

² Materials Genome Institute, Shanghai University, 333 Nanchen Road, Shanghai, 200444, P.R. China

³ Shanghai Advanced Research Institute, Chinese Academy of Sciences, Shanghai, 201210, P. R. China

⁴ These authors contributed equally.

Correspondence Email: S.Levchenko@skoltech.ru; gaoyi@zjlab.org.cn

Abstract

Single-atom metal alloy catalysts (SAACs) have recently become a very active new frontier in catalysis research. The simultaneous optimization of both facile dissociation of reactants and a balanced strength of intermediates' binding make them highly efficient and selective for many industrially important reactions. However, discovery of new SAACs is hindered by the lack of fast yet reliable prediction of the catalytic properties of the sheer number of candidate materials. In this work, we address this problem by applying a compressed-sensing data-analytics approach parameterized with density-functional inputs. Our approach is faster and more accurate than the current state-of-the-art linear relationships. Besides consistently predicting high efficiency of the experimentally studied Pd/Cu, Pt/Cu, Pd/Ag, Pt/Au, Pd/Au, Pt/Ni, Au/Ru, and Ni/Zn SAACs (the first metal is the dispersed component), we identify more than two hundred yet unreported candidates. Some of these new candidates are predicted to exhibit even higher stability and efficiency than the reported ones. Our study demonstrates the importance of breaking linear relationships to avoid bias in catalysis design, as well as provides a recipe for selecting best candidate materials from hundreds of thousands of transition-metal SAACs for various applications.

Recently, single-atom dispersion has been shown to dramatically reduce the usage of rare and expensive metals in heterogeneous catalysis, at the same time providing unique possibilities for tuning catalytic properties.^{1,2} The pioneering work by Sykes and co-workers² has demonstrated that highly dilute bimetallic alloys, where single atoms of Pt-group are dispersed on the surface of an inert metal host, are highly efficient and selective in numerous catalytic reactions. These alloy catalysts are now extensively used in the hydrogenation-related reactions such as hydrogenation of CO₂, water-gas shift reaction, hydrogen separation, and many others.³⁻⁵ The outstanding performance of SAACs is attributed to a balance between efficiency of H₂ dissociation and binding of H at the surface of metallic alloys.^{2,6,7}

Using desorption measurements in combination with high-resolution scanning tunneling microscopy, Kyriakou *et al.* have shown that isolated Pd atoms on a Cu surface can substantially reduce the energy barrier for both hydrogen uptake and subsequent desorption from the Cu metal surface.² Lucci and co-workers have observed that isolated Pt atoms on the Cu(111) surface

exhibit stable activity and 100% selectivity for the hydrogenation of butadiene to butenes.⁸ Liu *et al.* have investigated the fundamentals of CO adsorption on Pt/Cu SAAC using a variety of surface science and catalysis techniques. They have found that CO binds more weakly to single Pt atoms in Cu(111), compared to larger Pt ensembles or monometallic Pt. Their results demonstrate that SAACs offer a new approach to design CO-tolerant materials for industrial applications.⁹ To date, Pd/Cu,¹⁰⁻¹² Pt/Cu,^{7-9, 13-15} Pd/Ag,^{12, 16} Pd/Au,¹² Pt/Au,¹⁷ Pt/Ni,¹⁸ Au/Ru,¹⁹ and Ni/Zn²⁰ SAACs have been synthesized and found to be active and selective towards different hydrogenation reactions. However, the family of experimentally synthesized SAACs for hydrogenation remains small and comparisons of their catalytic properties are scarce.

Conventional approaches to design single-atom heterogeneous catalysts for different industrially relevant hydrogenation reactions mainly rely on trial-and-error methods. However, challenges in synthesis and *in situ* experimental characterization of SAACs impose limitations on these approaches. With advances in first-principles methods and computational resources, theoretical modeling is proven to provide new opportunities for rational catalyst design.^{6, 21-48} The general simple yet powerful approach is the creation of a large database with first-principles based inputs, followed by intelligent interrogation of the database in search of materials with the desired properties.^{35, 48} Significant efforts have been made in developing reliable descriptor-based models following the above general approach.^{6, 21-35, 48} In catalysis, a descriptor is a parameter (a feature) of the catalytic material that is easy to evaluate and is correlated with a complex target property (e.g., activation energy or turnover frequency of a catalytic reaction). A notable amount of research has been devoted to near-linear dependencies between descriptors and target properties.²²⁻³⁰ For example, the linear relationship between the reaction energies and the activation energies is known as the Brønsted-Evans-Polanyi relationship (BEP) in heterogeneous catalysis.^{29, 30, 45-47} Also, the linear correlation between *d*-band center of a clean transition-metal surface and adsorption energies of molecules on that surface have been studied in great detail and widely applied.^{22-24, 36, 44} In catalysis, near-linear correlations between adsorption energies of different adsorbates are referred to as scaling relations.^{26, 28, 37} The advantages of such correlations are their simplicity and usually strong physical foundations. However, they are not exact, and there is an increasing number of studies focused on overcoming limitations imposed by the corresponding approximations.^{6, 31-34, 38-41, 48} The nonlinear and intricate relationship between the catalysts' properties and surface reactions at realistic conditions^{42, 43} has held back the reliable description of catalytic properties. Note that, although the stability of SAACs is of no less significance in designing a potential catalyst than their catalytic performance, it hasn't received the same attention.

In this work, combining first-principles calculations and compressed-sensing data-analytics methodology, we address the issues that inhibit the wider use of SAAC in different industrially important reactions. By identifying descriptors based only on properties of the host surfaces and guest single atoms, we predict the binding energies of H (BE_H), the dissociation energy barriers of H₂ molecule (E_b), and the segregation energies (SE) of the single guest atom at different transition metal surfaces. The state-of-the-art compressed-sensing based approach employed here for identifying the key descriptive parameters is the recently developed SISSO (sure independence screening and sparsifying operator).⁴⁹ SISSO enables us to identify the best low-dimensional descriptor in an immensity of offered candidates. The computational time required for our models to evaluate the catalytic properties of a SAAC is reduced by at least a factor of

one thousand compared to first-principles calculations, which enables high-throughput screening of a huge number of SAAC systems.

Results

The BE_H for more than three hundred SAACs are calculated within the framework of DFT with RPBE exchange-correlation functional. This large dataset consists of BE_H values at different low-index surface facets including fcc(111), fcc(110), fcc(100), hcp(0001), and bcc(110) and three stepped surface facets including fcc(211), fcc(310), and bcc(210) of SAACs with twelve transition-metal hosts (Cu, Zn, Cr, Pd, Pt, Rh, Ru, Cd, Ag, Ti, Nb, and Ta). On each TM host surface, one of the surface atoms is substituted by a guest atom to construct the SAACs. H atom is placed at different non-equivalent high-symmetry sites close to the guest atom [Figure S1 in Supplementary Information (SI)], and the BE_H for the most favorable site is included in the data set. Complete information on adsorption sites and the corresponding BE_H is given in SI. The BE_H are further validated by a comparison with previous calculations.^{6, 21}

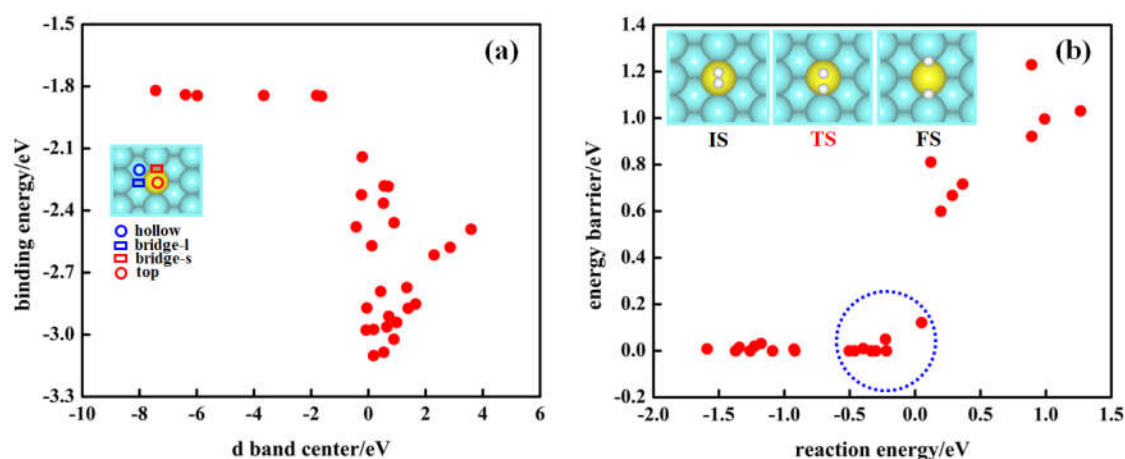


Figure 1. Correlation between (a) H-atom binding energy BE_H and the d -band center and (b) the H_2 dissociation energy barrier E_b and the H_2 dissociation reaction energy for Ag(110) based SAACs. The SAACs inside the blue dotted circle in (b) significantly reduce E_b while reducing reaction energy only moderately.

To better understand the variation in BE_H for different guest atoms, we first investigate correlation between BE_H and the d -band center for alloyed systems. The correlation is shown in Figure 1a for different SAACs on Ag(110) host surface. According to the d -band center theory,^{21, 23, 36, 44} the closer the d -band center is to the Fermi level, the stronger the BE_H should be. However, it is evident from Figure 1a that the expected linear correlation, as predicted by the d -band model, is broken for SAACs for H adsorption. This is due to the small size of the atomic H orbitals, leading to a relatively weak coupling between H s and the TM d -orbitals.²¹ Furthermore, we check the validity of the BEP relations between the E_b and the H_2 dissociation reaction energy for SAACs (Figure 1b), which is commonly used to extract kinetic data for a reaction on the basis of the adsorption energies of the reactants and products.^{29, 45-47} As shown in Figure 1b, the highlighted SAACs inside the blue dotted circle significantly reduce E_b while reducing reaction energy only moderately. As a result, SAACs provide small reaction energy and low activation energy barrier, which leads to breaking BEP relations and thus optimized catalytic

performance. The BEP relations are also found to be broken for other reactions catalyzed by SAACs.⁶

Table 1. Primary features used for the descriptor construction.

system	class	name	abbreviation	
host	atomic	Energy of the highest-occupied Kohn-Sham level	H*	
		Energy of the lowest-unoccupied Kohn-Sham level	L*	
		Electron affinity (Atomic radius)	EA*(R*) [#]	
		Ionization potential	IP*	
		Binding energy of H with single host metal atom (Binding energy of host metal dimers)	EH*(EB*) [#]	
		Binding distance of H with single host metal atom (Binding distance of host metal dimer)	dH*(dd*) [#]	
		bulk	Cohesive energy	EC*
	<i>d</i> -band center		DC*	
	surface [¶]		<i>d</i> -band center of the top surface layer	DT*
		<i>d</i> -band center of the subsurface layer	DS*	
		Slab Fermi level	F*	
	guest atom	atomic	Energy of the highest-occupied Kohn-Sham level	H
			Energy of the lowest-unoccupied Kohn-Sham level	L
Electron affinity (Atomic radius)			EA(R) [#]	
Ionization potential			IP	
Binding energy of H with single guest metal atom (Binding energy of guest metal dimers)			EH(EB) [#]	
Binding distance of H with single guest metal atom (Binding distance of guest metal dimers)			dH(dd) [#]	
bulk			Cohesive energy	EC
		<i>d</i> -band center	DC	

[#]the feature in parentheses is used for the model of segregation energy (SE), while the feature outside parentheses is used for the models of H binding energy (BE_H) and H₂ dissociation energy barrier (*E_b*). [¶]the surface-based primary features were calculated using the slab unit cell consisting of one atom per atomic layer.

Thus, the standard simple correlations (from *d*-band center theory and the BEP relations) fail for H adsorption on SAACs. Moreover, the calculation of the *d*-band center for each SAAC is highly computationally demanding, considering the very large number of candidates. These facts emphasize the necessity to find new accurate but low-cost descriptors for computational screening of SAACs. In the SISSO method, a huge pool of more than ten billion candidate features is first constructed iteratively by combining 19 low-cost primary features listed in Table 1 using a set of mathematical operators. A compressed-sensing based procedure is used to select

one or more most relevant candidate features and construct a linear model of the target property (see SI for details on the SISO procedure). Note that the three primary surface features are properties of the pure host surfaces (elemental metal systems). This is undoubtedly much more efficient than obtaining the properties of SAACs (alloyed metal systems). In the latter case, due to the interaction between the single guest atom and its images, a large supercell of the whole periodic system containing guest atom and host surface needs to be computed. On the contrary, only smallest unit cell is needed to compute the pristine surface features.

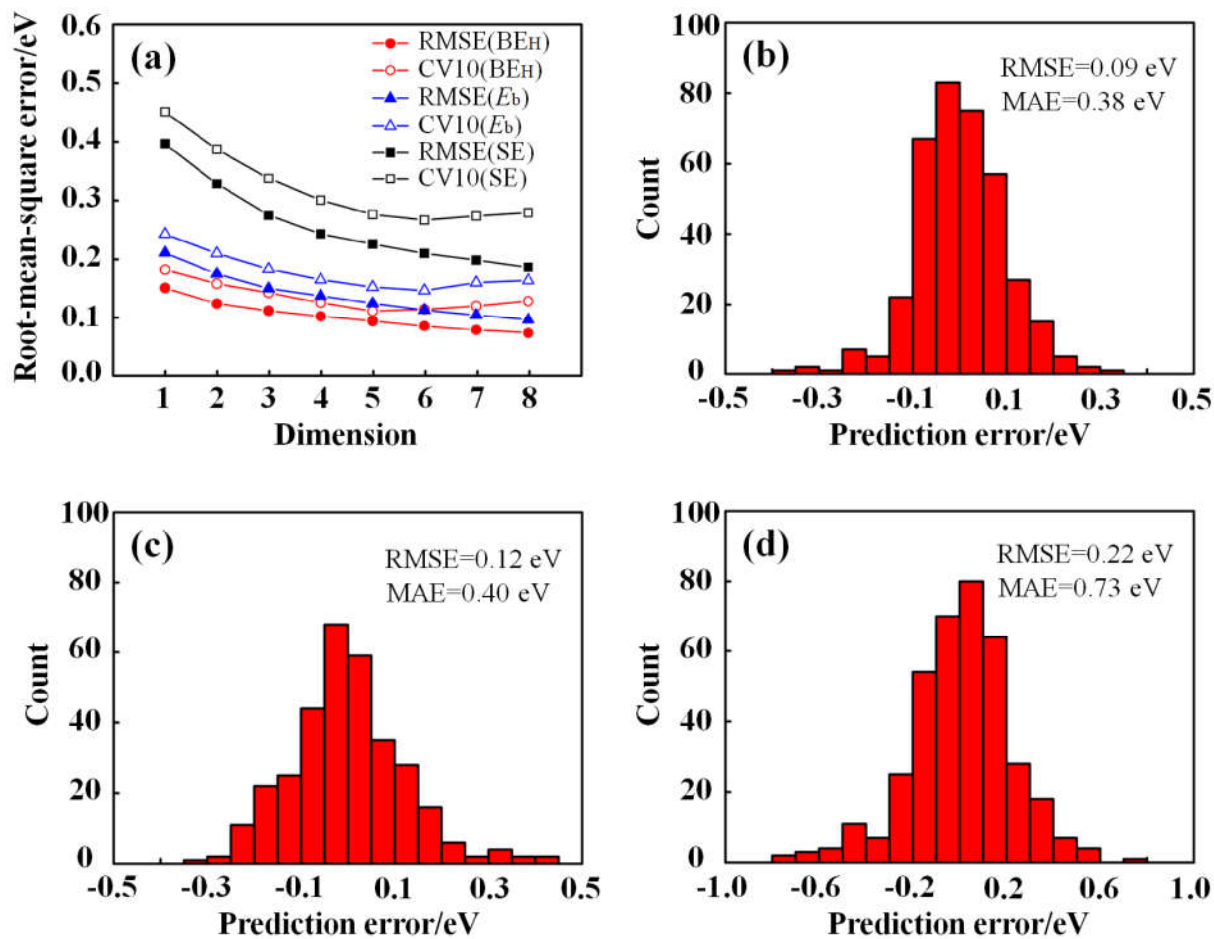


Figure 2. (a) RMSE and the averaged RMSE of the 10 fold cross-validation. (b-d) Distribution of errors for the best models versus RPBE results for BE_H (b), E_b (c), and SE (d).

To test the predictive power of obtained models, we employ 10-fold cross validation (CV10). The dataset is first split into 10 subsets, and the descriptor identification along with the model training is performed using 9 subsets. Then the error in predicting properties of the systems in the remaining subset is evaluated with the obtained model.⁵⁰⁻⁵² The CV10 error is defined as the average value of the test errors obtained for each of the ten subsets. In SISO over-fitting may occur with increasing dimensionality of the descriptor (i.e., the number of complex features that are used in construction of the linear model).⁴⁹ The descriptor dimension at which the CV10 error starts increasing identifies the optimal dimensionality of the descriptor (the detailed validation approaches have been discussed in the SI to confirm its reliability). The root-mean-

square errors (RMSE), together with the CV10 errors of the SISO models for BE_H , E_b , and SE are displayed in Figure 2a. The obtained optimal descriptor dimensionalities for BE_H , E_b , and SE of the SAACs are 5, 6, and 6, respectively. Distribution of errors for the best models versus RPBE results is displayed in Figure 2(b-d). The RMSE, and maximum absolute error (MAE) of the models are also shown. The error distributions for all the lower-dimensional models relative to the best ones are displayed in Figure S3-5.

Table 2. The identified descriptors and the coefficients in corresponding SISO models for BE_H , E_b , and SE.

property	d^m	descriptor	coefficient
BE_H	d_1^5	$(EA^*+2F-EC)\cdot DT^*\cdot EH^*/(EC^*+F^*)$	0.12653E+00
	d_2^5	$\sqrt[3]{DC}\cdot H^*\cdot DT^*\cdot (EA^*-EH^* - EC-EC^*)$	-0.20440E-02
	d_3^5	$ EH^*-L^*- EH-F^* /(DC^2+EC\cdot EC^*)$	-0.50891E+00
	d_4^5	$ EH-F^*-EH^* - EC^*-EC- DT^*-F^* $	0.34705E-01
	d_5^5	$L\cdot EC\cdot (EA^*+DS^*- H-EH / L^*-EH^* $	-0.48772E-04
E_b	d_1^6	$ ((IP^*-L)- EC^*-DT^*)/ EC/DC-L^*/IP^* $	-0.87339E-01
	d_2^6	$(EA^*+DC^*+ DC-DT^*)/(EA^*+EH^*+ L^*-F^*)$	-0.19577E-01
	d_3^6	$(DC+EH^*)\cdot (EC^*-F^*)\cdot (L-EC - EC-EH)$	-0.13173E-01
	d_4^6	$(DT^*-EH)\cdot DC\cdot (H/EC+EA^*/L^*)/EC^*$	-0.19172E-01
	d_5^6	$e^{EC}\cdot EH\cdot DS^*/((L^*-DS^*)+ H^*-EC^*)$	0.33549E-01
	d_6^6	$DC^2\cdot (EC^*-F^*)/(DT^*-F^*-EA+EC)$	-0.14362E-02
SE	d_1^6	$(EC+IP+ F^*-DT^*)/(IP^*/R+H^*/dd^*)$	-0.82665E+00
	d_2^6	$ DC-EB^* \cdot (L-DC-EC)/EB^2$	0.30742E+00
	d_3^6	$ EC^*-L^*+ DC-DS^* - DC-F^* - EC-F^* $	0.11317E+00
	d_4^6	$ H-IP-L+IP^* /((DC/EC)+(EC/H))$	0.17455E+00
	d_5^6	$(F^*-EC)\cdot (L^*-DT^*-IP)/(F^*-EB^*)$	-0.51761E-02
	d_6^6	$EC^*\cdot DC\cdot (EB^*-L)\cdot (L+L^*-EC-DS^*)$	-0.80032E-03

From the Table 2 one can see that the d -band center features DC, DC*, DT, DT*, DS, and DS* appear in every dimension of the descriptors for BE_H and E_b , consistent with the well-established importance of d -band center for adsorption at transition-metal surfaces.^{21, 23, 36, 44} The cohesive energies of guest (EC) and host (EC*) bulk metals are selected in each dimension of the descriptor for SE. This is due to the fact that the segregation is driven by the imbalance of binding energy between host and guest-host atoms. Interestingly, most of the descriptor components include only simple mathematical operators (+, -, ·, /, ||), indicating that the primary features already capture most of the complexity of the target properties.

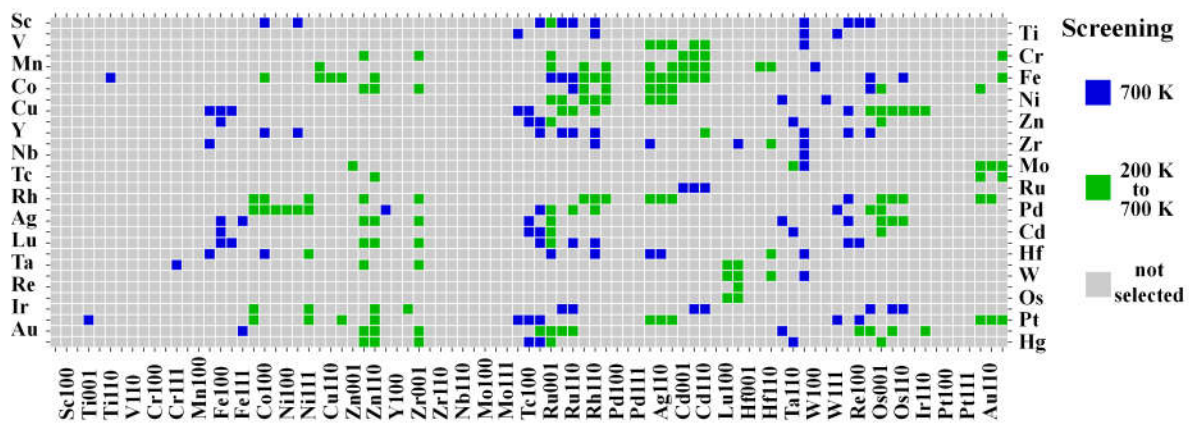
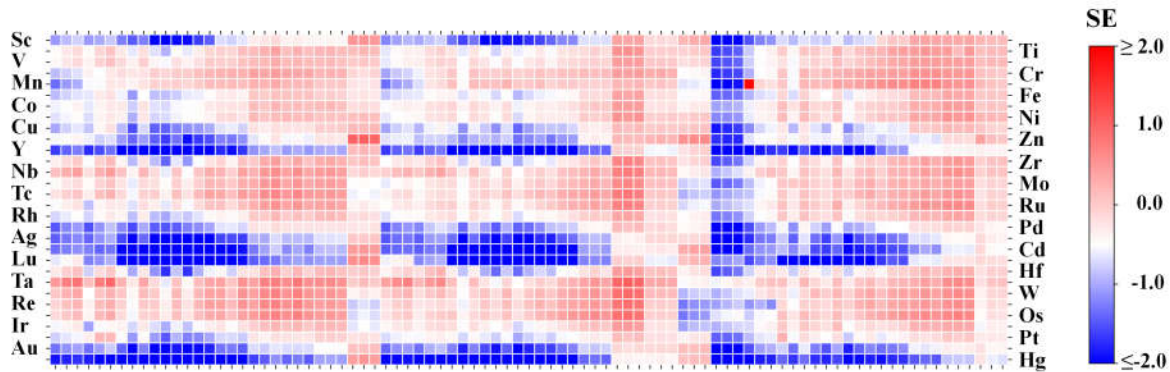
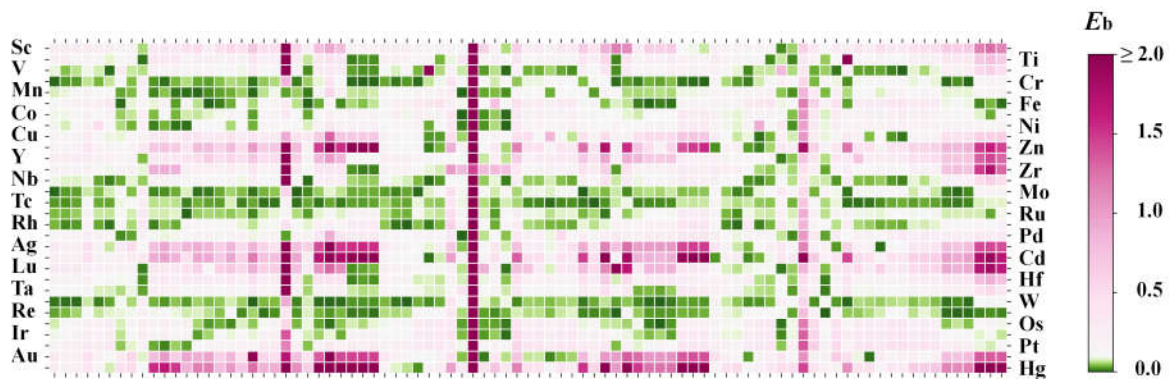
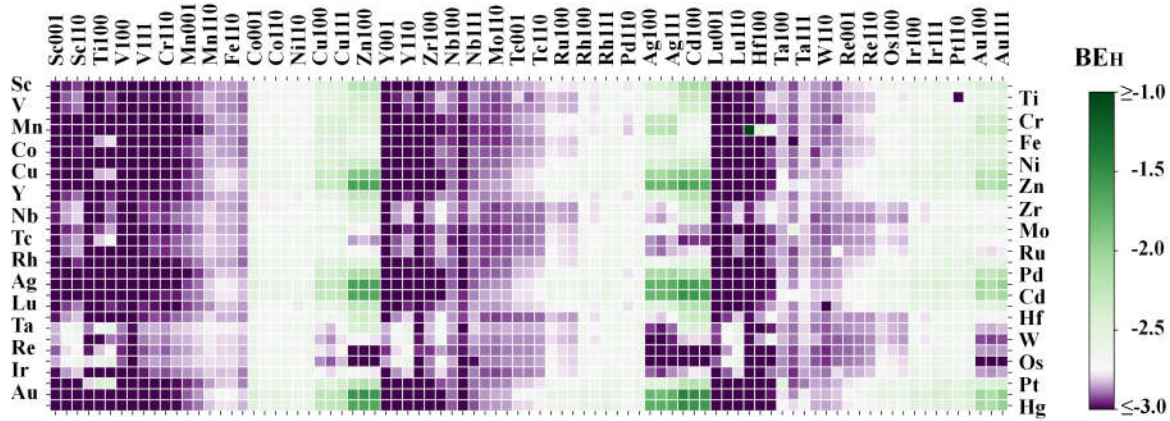


Figure 3. High-throughput screening of SAACs for (a) BE_H , (b) E_b , and (c) SE. The promising candidates at different temperatures T are highlighted in (d). Vertical axis displays the guest atom type, and the horizontal axis displays the host metal surfaces with different surface cuts.

We employ the identified computationally cheap SISSO models to perform high-throughput screening of SAACs to find the best candidates for the hydrogenation reactions. The results for BE_H , E_b , and SE of the flat surfaces are displayed in Figure 4 a-c (see Figure S6 for the results for the stepped surfaces, the values of BE_H , E_b , and SE for all the SAACs are given in SI.).

The choice of the screening criteria for the three properties BE_H , E_b , and SE, which are related to the activity and stability of SAACs, plays the central role in the screening processes and determines the candidates to be chosen. Previous work demonstrates that for the high performance in hydrogenation reactions, SAACs should exhibit weaker binding of H and lower H_2 dissociation energy barrier simultaneously.² However, different criteria are applicable for different reaction conditions. For example, at low temperatures SAACs can maintain their stability for a longer time. At higher temperatures H atoms will desorb from the surfaces and larger energy barriers can be overcome, resulting in a requirement for stronger binding and higher upper limit of the dissociation barrier E_b . Keeping this variability in mind, we consider temperature and pressure-dependent selection criteria (see methods part for details on the selection criteria). We have screened more than five thousand SAAC candidates (including about the same number of flat and stepped surfaces; the values of the primary features for all the candidates can be found in the SI) at both low temperature (200 K) and high temperature (700 K) at partial H_2 pressure $p = 1$ atm. We find 160 flat-surface SAACs (Figure 3d, in green) and 134 stepped-surface SAACs (Figure S6d, in green) that are both active and stable at a low temperature (200 K). At a higher temperature (700 K), 102 flat-surface SAACs (Figure 3d, in blue and green) and 136 stepped-surface SAACs (Figure S6d, in blue and green) are classified as promising SAACs for hydrogenation reactions. Moreover, we have identified the SAACs which are promising in a wide range of temperatures (green squares in Figure 3d for flat surfaces and Figure S6d for stepped surfaces).

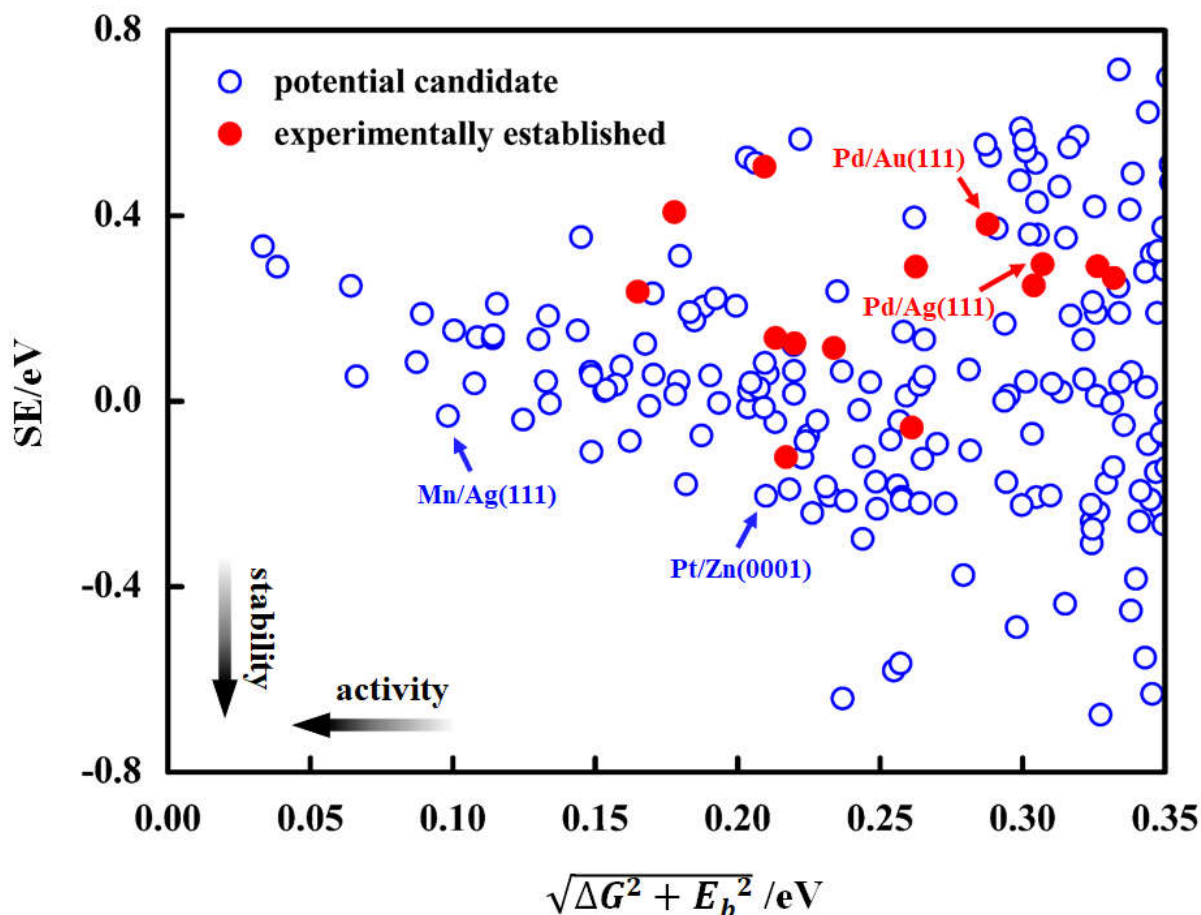


Figure 4. Stability vs. activity map for flat SAACs surfaces at $T = 298\text{ K}$ and $p = 1\text{ atm}$. The SE on y-axis represents stability and activity parameter $\sqrt{\Delta G^2 + E_b^2}$ is shown on x-axis. Experimentally established SAACs are denoted with red solid spheres and the blue open circles represent new predicted candidates.

Note that, without the stability selection criterion based on SE, all experimentally established SAACs (Pd/Cu, Pt/Cu, Pd/Ag, Pd/Au, Pt/Au, Pt/Ni, Au/Ru, Ni/Zn) are predicted to be good catalysts in the temperature range of $200\text{ K} < T < 700\text{ K}$, which are further confirmed by DFT calculations. However, some of these systems (Pd/Ag and Pd/Au) are experimentally shown to have low stability.^{12, 16} Thus, inclusion of the stability-related property SE is of immense importance for a reliable prediction of catalytic performance, as is confirmed by our results. We define an activity (or efficiency) indicator involving both the free energy of H adsorption (ΔG) and the energy barrier (E_b) as $\sqrt{\Delta G^2 + E_b^2}$ to construct an activity-stability map. As shown in Figure 4, some of the new discovered candidates (bottom-left corner of activity-stability map) are predicted to have both higher stability and efficiency than the reported ones, making them perfectly optimized for practical applications (see Figure S7 for the results for the stepped surfaces). Considering stability, activity, and abundance, two discovered best candidates Mn/Ag(111) and Pt/Zn(0001) are highlighted in Figure 4.

In summary, by combining first-principles calculations and the data-analytics approach SISO, we have identified accurate and reliable models for the description of the hydrogen binding energy, dissociation energy, and guest-atom segregation energy for SAACs, which allow us to make fast yet reliable prediction of the catalytic performance of hundreds of thousands SAACs in hydrogenation reactions. The model correctly evaluates performance of experimentally tested SAACs. By scanning more than five thousand SAACs with our model, we have identified over two hundred new SAACs with both improved stability and performance compared to the existing ones. Our approach can be easily adapted to designing new functional materials for various applications.

Methods

All first-principles calculations are performed with the revised Perdew-Burke-Ernzerhof (RPBE) functional⁵³ as implemented in the all-electron full-potential electronic-structure code FHI-aims.⁵⁴ The choice of functional is validated based on a comparison of calculated H₂ adsorption energies to the available experimental results⁵⁵ (see Table S1). Nevertheless, it is expected that, because of the large set of systems inspected and the small variations introduced by the functional choice, the main trends will hold even when using another functional (see Supporting Information (SI) for more details on the computational setup). The climbing-image nudged elastic band (CI-NEB) algorithm is employed to identify the transition state structures.⁵⁶

BE_H are calculated using equation (1), where $E_{H/support}$ is the energy of the total H/support system, $E_{support}$ is the energy of the metal alloy support, and E_H is the energy of an isolated H atom.

$$BE_H = E_{H/support} - E_{support} - E_H \quad (1)$$

The surface segregation energy in the dilute limit, SE, is defined as the energy difference of moving the single impurity from the bulk to the surface when surface H adatom is present (the H is put at the most stable adsorption site for each system). In this work, it is calculated using equation (2), where $E_{top-layer}$ and $E_{nth-layer}$ correspond to the total RPBE energy of the slab with the impurity in the top and n th surface layer, respectively. The value of n is chosen so that the energy difference between $E_{nth-layer}$ and $E_{(n-1)th-layer}$ is less than 0.05 eV.

$$SE = E_{surface} - E_{nth-layer} \quad (2)$$

Using first-principles inputs as training data, we have employed SISO to single out a simple and physically intuitive descriptor from a huge number of potential candidates. In practice, a huge pool of more than ten billion candidate descriptors is first constructed iteratively by combining user-defined primary features with a set of mathematical operators. The number of times the operators are applied determines the complexity of the resulting descriptors. We consider up to three levels of complexity (feature spaces) Φ_1 , Φ_2 , and Φ_3 . Note that a given feature space Φ_n also contains all of the lower rung (i.e. $n-1$) feature spaces. Subsequently, the desired low-dimensional representation is obtained from this pool.⁴⁹ The details of the feature space (Φ_n) construction and the descriptor identification processes can be found in the SI. The proper selection of primary features is crucial for the performance of SISO-identified descriptors. Inspired by previous studies,^{31, 38} we consider three classes of primary features (see

Table 1) related to the metal atom, bulk, and surface. The more detailed description and values of all the primary features are given in the SI.

The selection of the promising candidates at various temperatures and hydrogen partial pressures is performed based on *ab initio* atomistic thermodynamics.⁵⁷ H adsorption/desorption on SAAC surfaces as a function of temperature and H₂ partial pressure (T, p) is characterized by the free energy of adsorption ΔG :

$$\Delta G = E_{\text{H/support}} - E_{\text{support}} - \mu_{\text{H}}(T, p)$$

with the chemical potential of hydrogen $\mu_{\text{H}} = \frac{1}{2}\mu_{\text{H}_2}$ obtained from:

$$\mu_{\text{H}} = \frac{1}{2} \left(E_{\text{H}_2} + \Delta\mu_{\text{H}_2}(T, p) \right)$$

where $\Delta\mu_{\text{H}_2}(T, p) = \mu_{\text{H}_2}(T, p^0) - \mu_{\text{H}_2}(T^0, p^0) + k_B T \ln\left(\frac{p}{p^0}\right)$.

Here $T^0 = 298 \text{ K}$ and $p^0 = 1 \text{ atm}$. The first two terms are taken from JANAF thermochemical tables.⁵⁸ In the following, we set $p = 1 \text{ atm}$.

According to Sabatier principle the optimum heterogeneous catalyst should bind the reactants strong enough to allow for adsorption, but also weak enough to allow for the consecutive desorption.²⁵ In this work, a BE_{H} range is defined by the conditions:

$$\left| \text{BE}_{\text{H}} - \frac{1}{2}(E_{\text{H}_2} - 2E_{\text{H}}) - \frac{1}{2}\Delta\mu_{\text{H}_2}(T) \right| < 0.3 \text{ eV}$$

where $E_{\text{H}_2} - 2E_{\text{H}}$ is the hydrogen binding energy of the hydrogen molecule. The experimental value of -4.52 eV ⁵⁹ was used in this work.

The above conditions correspond to the free-energy bounds:

$$|\Delta G| < 0.3 \text{ eV},$$

Conditions on energy barrier (E_{b}) are defined by considering Arrhenius-type behaviour of the reaction rate on E_{b} and T . Assuming that acceptable barriers are below 0.3 eV for $T^0 = 298 \text{ K}$, we estimate acceptable barrier at any temperature as $E_{\text{b}} < \frac{0.3T}{T^0} \text{ eV}$.

Similarly the bounds for SE are determined by imposing a minimum 10% ratio for top-layer to subsurface-layers dopant concentration by assuming an Arrhenius-type relation with SE interpreted as activation energy:

$$\text{SE} < k_B T \ln(10)$$

References

1. Qiao, B. et al. Single-atom catalysis of CO oxidation using Pt₁/FeOx. *Nature Chemistry* **3**, 634 (2011).
2. Kyriakou, G. et al. Isolated metal atom geometries as a strategy for selective heterogeneous hydrogenations. *Science* **335**, 1209-1212 (2012).
3. Choi, K.I. & Vannice, M.A. CO oxidation over Pd and Cu catalysts V. Al₂O₃-supported bimetallic Pd/Cu particles. *Journal of Catalysis* **131**, 36-50 (1991).

4. Greeley, J., Nørskov, J.K., Kibler, L.A., El - Aziz, A.M. & Kolb, D.M. Hydrogen evolution over bimetallic systems: Understanding the trends. *ChemPhysChem* **7**, 1032-1035 (2006).
5. Kamakoti, P. et al. Prediction of hydrogen flux through sulfur-tolerant binary alloy membranes. *Science* **307**, 569-573 (2005).
6. Darby, M.T., Réocreux, R., Sykes, E.C.H., Michaelides, A. & Stamatakis, M. Elucidating the stability and reactivity of surface intermediates on single-atom alloy catalysts. *ACS Catalysis* **8**, 5038-5050 (2018).
7. Sun, G. et al. Breaking the scaling relationship via thermally stable Pt/Cu single atom alloys for catalytic dehydrogenation. *Nature Communications* **9**, 1-9 (2018).
8. Lucci, F.R. et al. Selective hydrogenation of 1, 3-butadiene on platinum–copper alloys at the single-atom limit. *Nature Communications* **6**, 1-8 (2015).
9. Liu, J. et al. Tackling CO poisoning with single-atom alloy catalysts. *Journal of the American Chemical Society* **138**, 6396-6399 (2016).
10. Tierney, H.L., Baber, A.E. & Sykes, E.C.H. Atomic-scale imaging and electronic structure determination of catalytic sites on Pd/Cu near surface alloys. *The Journal of Physical Chemistry C* **113**, 7246-7250 (2009).
11. Boucher, M.B. et al. Single atom alloy surface analogs in Pd_{0.18}Cu₁₅ nanoparticles for selective hydrogenation reactions. *Physical Chemistry Chemical Physics* **15**, 12187-12196 (2013).
12. Pei, G.X. et al. Performance of Cu-alloyed Pd single-atom catalyst for semihydrogenation of acetylene under simulated front-end conditions. *ACS Catalysis* **7**, 1491-1500 (2017).
13. Marcinkowski, M.D. et al. Selective formic acid dehydrogenation on Pt-Cu single-atom alloys. *ACS Catalysis* **7**, 413-420 (2017).
14. Simonovis, J.P., Hunt, A., Palomino, R.M., Senanayake, S.D. & Waluyo, I. Enhanced stability of Pt-Cu single-atom alloy catalysts: in situ characterization of the Pt/Cu(111) surface in an ambient pressure of CO. *The Journal of Physical Chemistry C* **122**, 4488-4495 (2018).
15. Marcinkowski, M.D. et al. Pt/Cu single-atom alloys as coke-resistant catalysts for efficient C–H activation. *Nature Chemistry* **10**, 325 (2018).
16. Pei, G.X. et al. Ag alloyed Pd single-atom catalysts for efficient selective hydrogenation of acetylene to ethylene in excess ethylene. *ACS Catalysis* **5**, 3717-3725 (2015).
17. Duchesne, P.N. et al. Golden single-atomic-site platinum electrocatalysts. *Nature Materials* **17**, 1033-1039 (2018).
18. Li, Z. et al. Atomically dispersed Pt on the surface of Ni particles: synthesis and catalytic function in hydrogen generation from aqueous ammonia–borane. *ACS Catalysis* **7**, 6762-6769 (2017).
19. Chen, C.H. et al. Ruthenium - Based Single-Atom Alloy with High Electrocatalytic Activity for Hydrogen Evolution. *Advanced Energy Materials* **9**, 1803913 (2019).
20. Studt, F. et al. Identification of non-precious metal alloy catalysts for selective hydrogenation of acetylene. *Science* **320**, 1320-1322 (2008).
21. Greeley, J. & Mavrikakis, M. Alloy catalysts designed from first principles. *Nature Materials* **3**, 810-815 (2004).
22. Pallassana, V., Neurock, M., Hansen, L.B., Hammer, B. & Nørskov, J.K. Theoretical analysis of hydrogen chemisorption on Pd(111), Re(0001) and Pd ML/Re(0001), Re ML/Pd(111) pseudomorphic overlayers. *Physical Review B* **60**, 6146 (1999).

23. Mavrikakis, M., Hammer, B. & Nørskov, J.K. Effect of strain on the reactivity of metal surfaces. *Physical Review Letters* **81**, 2819 (1998).
24. Xin, H., Vojvodic, A., Voss, J., Nørskov, J.K. & Abild-Pedersen, F. Effects of *d*-band shape on the surface reactivity of transition-metal alloys. *Physical Review B* **89**, 115114 (2014).
25. Nørskov, J.K., Bligaard, T., Rossmeisl, J. & Christensen, C.H. Towards the computational design of solid catalysts. *Nature Chemistry* **1**, 37 (2009).
26. Montemore, M.M. & Medlin, J.W. Scaling relations between adsorption energies for computational screening and design of catalysts. *Catalysis Science & Technology* **4**, 3748-3761 (2014).
27. Greeley, J. Theoretical heterogeneous catalysis: scaling relationships and computational catalyst design. *Annual Review of Chemical and Biomolecular Engineering* **7**, 605-635 (2016).
28. Abild-Pedersen, F. et al. Scaling properties of adsorption energies for hydrogen-containing molecules on transition-metal surfaces. *Physical Review Letters* **99**, 016105 (2007).
29. Michaelides, A. et al. Identification of general linear relationships between activation energies and enthalpy changes for dissociation reactions at surfaces. *Journal of the American Chemical Society* **125**, 3704-3705 (2003).
30. Logadottir, A. et al. The Brønsted–Evans–Polanyi relation and the volcano plot for ammonia synthesis over transition metal catalysts. *Journal of Catalysis* **197**, 229-231 (2001).
31. Andersen, M., Levchenko, S.V., Scheffler, M. & Reuter, K. Beyond scaling relations for the description of catalytic materials. *ACS Catalysis* **9**, 2752-2759 (2019).
32. Calle-Vallejo, F., Loffreda, D., Koper, M.T. & Sautet, P. Introducing structural sensitivity into adsorption–energy scaling relations by means of coordination numbers. *Nature Chemistry* **7**, 403 (2015).
33. O’Connor, N.J., Jonayat, A., Janik, M.J. & Senftle, T.P. Interaction trends between single metal atoms and oxide supports identified with density functional theory and statistical learning. *Nature Catalysis* **1**, 531-539 (2018).
34. Xu, H., Cheng, D., Cao, D. & Zeng, X.C. A universal principle for a rational design of single-atom electrocatalysts. *Nature Catalysis* **1**, 339-348 (2018).
35. Curtarolo, S. et al. The high-throughput highway to computational materials design. *Nature Materials* **12**, 191-201 (2013).
36. Hammer, B. & Nørskov, J.K. Why gold is the noblest of all the metals. *Nature* **376**, 238-240 (1995).
37. Roling, L.T. & Abild - Pedersen, F. Structure-Sensitive Scaling Relations: Adsorption Energies from Surface Site Stability. *ChemCatChem* **10**, 1643-1650 (2018).
38. Li, Z., Wang, S., Chin, W.S., Achenie, L.E. & Xin, H. High-throughput screening of bimetallic catalysts enabled by machine learning. *Journal of Materials Chemistry A* **5**, 24131-24138 (2017).
39. Tran, K. & Ulissi, Z.W. Active learning across intermetallics to guide discovery of electrocatalysts for CO₂ reduction and H₂ evolution. *Nature Catalysis* **1**, 696-703 (2018).
40. Kitchin, J.R. Machine learning in catalysis. *Nature Catalysis* **1**, 230-232 (2018).
41. Li, Z., Wang, S. & Xin, H. Toward artificial intelligence in catalysis. *Nature Catalysis* **1**, 641-642 (2018).

42. Reuter, K. Ab initio thermodynamics and first-principles microkinetics for surface catalysis. *Catalysis Letters* **146**, 541-563 (2016).
43. Reuter, K., Frenkel, D. & Scheffler, M. The steady state of heterogeneous catalysis, studied by first-principles statistical mechanics. *Physical Review Letters* **93**, 116105 (2004).
44. Nørskov, J. Catalysis—Calculations and Concepts. *Advances in Catalysis: Impact of Surface Science on Catalysis* **45**, 71 (2001).
45. Van Santen, R.A., Neurock, M. & Shetty, S.G. Reactivity theory of transition-metal surfaces: a Brønsted–Evans–Polanyi linear activation energy– free-energy analysis. *Chemical Reviews* **110**, 2005-2048 (2009).
46. Fajín, J.L., Cordeiro, M.N.D., Illas, F. & Gomes, J.R. Generalized Brønsted–Evans–Polanyi relationships and descriptors for O–H bond cleavage of organic molecules on transition metal surfaces. *Journal of Catalysis* **313**, 24-33 (2014).
47. Viñes, F., Vojvodic, A., Abild-Pedersen, F. & Illas, F. Brønsted–Evans–Polanyi relationship for transition metal carbide and transition metal oxide surfaces. *The Journal of Physical Chemistry C* **117**, 4168-4171 (2013).
48. Zhong, M. et al. Accelerated discovery of CO₂ electrocatalysts using active machine learning. *Nature* **581**, 178-183 (2020).
49. Ouyang, R., Curtarolo, S., Ahmetcik, E., Scheffler, M. & Ghiringhelli, L.M. SISSO: A compressed-sensing method for identifying the best low-dimensional descriptor in an immensity of offered candidates. *Physical Review Materials* **2**, 083802 (2018).
50. Bengio, Y. & Grandvalet, Y. No unbiased estimator of the variance of k-fold cross-validation. *Journal of Machine Learning Research* **5**, 1089-1105 (2004).
51. Rodriguez, J.D., Perez, A. & Lozano, J.A. Sensitivity analysis of k-fold cross validation in prediction error estimation. *IEEE Transactions on Pattern Analysis and Machine Intelligence* **32**, 569-575 (2009).
52. Wong, T.-T. Performance evaluation of classification algorithms by k-fold and leave-one-out cross validation. *Pattern Recognition* **48**, 2839-2846 (2015).
53. Hammer, B., Hansen, L.B. & Nørskov, J.K. Improved adsorption energetics within density-functional theory using revised Perdew-Burke-Ernzerhof functionals. *Physical Review B* **59**, 7413 (1999).
54. Blum, V. et al. Ab initio molecular simulations with numeric atom-centered orbitals. *Computer Physics Communications* **180**, 2175-2196 (2009).
55. Silbaugh, T.L. & Campbell, C.T. Energies of formation reactions measured for adsorbates on late transition metal surfaces. *The Journal of Physical Chemistry C* **120**, 25161-25172 (2016).
56. Henkelman, G., Uberuaga, B.P. & Jónsson, H. A climbing image nudged elastic band method for finding saddle points and minimum energy paths. *The Journal of Chemical Physics* **113**, 9901-9904 (2000).
57. Reuter, K., Stampf, C. & Scheffler, M. Handbook of Materials Modeling 149-194 (Springer, 2005).
58. Tables, J.T. National Bureau of Standards Publication. *Washington, DC* (1971).
59. Lide, D.R. CRC handbook of chemistry and physics: a Ready-Reference Book of Chemical and Physical Data. (CRC press, 1995).

Acknowledgments

S.V.L. is supported by Skolkovo Foundation Grant.

Y.G. is supported by the National Natural Science Foundation of China (11604357, 11574340).

R.O. is supported by the National Key Research and Development Program of China (2018YFB0704400) and the Program of Shanghai Youth Oriental Scholars.

Author contributions

S.V.L. created the idea and conceived the work. S.V.L. and Y.G. designed and supervised the project. Z.-K.H. performed all the calculations. Z.-K.H., D.S., O.R., Y.G., and S.V.L. co-wrote the manuscript. All authors contributed to the analysis and interpretation of the results. All the authors commented on the manuscript and have given approval to the final version of the manuscript.

Competing interests

The authors declare no competing financial interests.

Additional information

Supplementary Information is available for this paper at <http://www.nature.com/nature>.

Correspondence and requests for materials should be addressed to S.V.L. or Y.G.

Single-Atom Alloy Catalysts Designed by First-Principles Calculations and Artificial Intelligence

Zhong-Kang Han,^{1,4} Debalaya Sarker,^{1,4} Runhai Ouyang,^{2,4} Yi Gao,^{3*} Sergey V. Levchenko^{1*}

¹ Center for Energy Science and Technology, Skolkovo Institute of Science and Technology, Skolkovo Innovation Center, Moscow, 143026, Russia

² Materials Genome Institute, Shanghai University, 333 Nanchen Road, Shanghai, 200444, P.R. China

³ Shanghai Advanced Research Institute, Chinese Academy of Sciences, Shanghai, 201210, P. R. China

⁴ These authors contributed equally.

Correspondence Email: S.Levchenko@skoltech.ru; gaoyi@sinap.ac.cn

S1. Computational details

All *ab initio* calculations were performed with the revised Perdew-Burke-Ernzerhof (RPBE) functional¹ as implemented in the all-electron full-potential electronic-structure code FHI-aims² using density-functional theory (DFT) and numerical atom-centered basis functions. The numerical settings are so chosen for the present study that a convergence better than 10^{-3} eV/atom in energy differences is achieved. The standard ‘tight’ settings (grids and basis functions) were employed which deliver the adsorption energies with basis-set superposition errors below 0.07 eV per adsorbed molecule. The choice of functional is validated based on a comparison of calculated H₂ adsorption energies to the available experimental results³ (Table S1). Spin-polarization effects are tested for and included where appropriate. Slabs of at least nine metal layers were considered with the two to four bottom layers fixed, based on the convergence of BE_H and SE (within 0.05 eV) with respect to the thickness and supercell size of the slab. The lattice vector along the direction parallel to the vacuum gap was 50 Å. All atoms in the systems except for the fixed bottom have been allowed to relax until the maximum remaining force fell below 10^{-2} eV/Å. The climbing-image nudged elastic band (CI-NEB) algorithm is employed to identify the transition state structures.⁴ H atom is placed at different non-equivalent high-symmetry sites close to the guest atom (Figure S1), and the BE_H for the most favorable site is included in the data set. The host metal surfaces considered in this work to construct the training data set are Cu(100), Cu(310), Zn(0001), Cr(110), Pd(111), Pd(211), Pt(111), Rh(111), Ru(0001), Cd(0001), Ag(100), Ag(110), Ti(0001), Nb(210), and Ta(210) with more than three hundred points for each considered properties. All the DFT calculated BE_H, SE, and E_b can be found in the file “data.txt”.

S2. Additional SISSO computational details

For constructing the Φ_1 , Φ_2 , and Φ_3 feature spaces we made use of the set of algebraic/functional operators given in eq. 1.

$$\hat{H}^{(m)} \equiv \{+, -, \cdot, /, \log, \exp, \exp^{-1}, ^2, ^3, \sqrt{\cdot}, \sqrt[3]{\cdot}, |-\cdot|\}, \quad (1)$$

The superscript m indicates that when applying $\hat{H}^{(m)}$ to primary features φ_1 and φ_2 a dimensional analysis is performed, which ensures that only physically meaningful combinations are retained

(e.g. only primary features with the same unit are added or subtracted). All primary features included in this study were obtained either from the literature (see Table S2), or from DFT calculations (see Table S3). The values of the primary features for the training data sets can be found in the file “data.txt” and the values of the primary features for all the high-throughput screening SAAC candidates can be found in the file “high-throughput-data.txt”.

The sparsifying ℓ_0 constraint is applied to a smaller feature subspace selected by a screening procedure (sure independence screening (SIS)), where the size of the subspace is equal to a user-defined SIS value times the dimension of the descriptor. The SIS value is not an ordinary hyperparameter and its optimization through a validation data set is not straightforward. Ideally, one would want to search the entire feature space for the optimal descriptor. However, this is not computationally tractable since the computational cost of the sparsifying ℓ_0 constraint grows exponentially with the size of the searched feature space. Instead, the SIS value should be chosen as large as computationally possible. The reasonable SIS values were chosen based on the convergence of the training error.

To confirm the reliability of the SISO model optimization approaches, the data were initially divided into training and test sets. The Pd(211) and Pt(111) based systems are used as test set while all the other data were contained in the training set. As mentioned in the main text, 10-fold cross validation (CV10) method was used to determine the dimensionality of the descriptor. First, the best descriptors were selected by SISO based on only the training data. The RMSR and CV10 errors on the training set for the descriptors of BE_H , E_b , and SE are displayed in Figure S2a. Second, the predictive power of the SISO selected descriptors was tested using the test set. We display in Figure S2b the distribution of errors on the training set and test set for the descriptors of BE_H (green box), E_b (blue box), and SE (cyan box). To check the predictive power of SISO selected descriptors on different types of surfaces, we divide the test set into two groups: one with only flat surface and the other one with only stepped surface. In the first group, we considered a new transition metal of Pt which are not contained in the training set (Cu, Zn, Cr, Pd, Rh, Ru, Cd, Ag, Ti, Nb, and Ta), while in the second group, we considered a new surface cut of fcc(211) which is also not included in the training set. The root-mean-square errors, RMSEs, (maximum absolute errors, MAEs) of the SISO selected descriptors for the test flat surface set are found to be BE_H : 0.10 eV (0.43 eV), E_b : 0.12 eV (0.62 eV), and SE: 0.22 eV (0.78 eV), while for the test stepped surface set are found to be BE_H : 0.11 eV (0.54 eV), E_b : 0.14 eV (0.71 eV), and SE: 0.24 eV (0.87 eV). The moderate errors of the RMSEs for both test flat surface set and test stepped surface set showed that the transferability of the descriptors is good. The little larger RMSEs and MAEs for test stepped surface set compared to that for test flat surface set can be rationalized by the fact that in the training set, more flat surfaces are considered compared to stepped surfaces. We would expect the errors for the test set to further decrease when more data are included in the training set. Thus, after confirming the reliability of the of the SISO model optimization approaches, finally we included all the data into the training set for the SISO selection of the best descriptors. As mentioned in the main text, the obtained optimal descriptor dimensionalities for BE_H , E_b , and SE of the SAACs are 5, 6, and 6, respectively. The same optimal descriptor dimensionalities for BE_H , E_b , and SE were found when the Pt(111) and Pd(211) based systems are not included, further confirming the reliability the used SISO model optimization approaches. The error distributions for all the lower dimensional models are displayed in Figure S3-5. The RMSE and MAE of the models are also shown. The

identified lower-dimensional descriptors and the coefficients in corresponding SISSO models for BE_H , E_b , and SE can be found in the file “descriptor.txt”. The top five largest deviations between calculated and predicted BE_H , E_b , and SE are collected in Table S4. As can be seen, the deviation for SE is larger than that of BE_H and E_b . However, we found even for SE our model’s precision is higher than 95% (Table S5).

Table S1. The experimental and theoretical adsorption energies (in eV) of H_2 at different transition metal surfaces.

method	Pt(111)	Ru(0001)	Pd(111)
RPBE	-0.56	-1.06	-1.01
PBE	-0.32	-0.78	-0.70
Experiments ³	-0.75	-1.20	-0.91

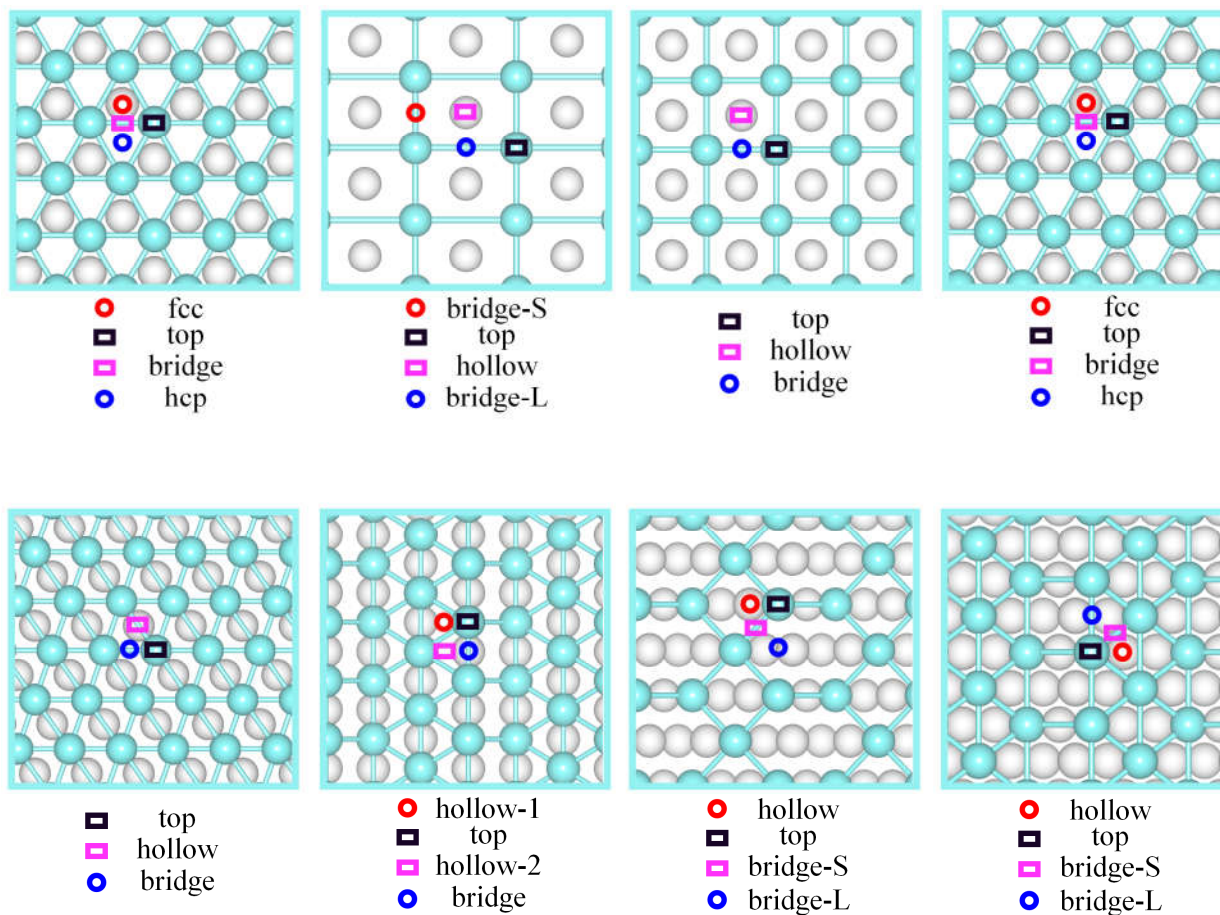


Figure S1. The considered hydrogen adsorption sites on the fcc(111) (a), fcc(110) (b), fcc(100) (c), hcp(0001) (d), bcc(110) (e), fcc(211) (f), fcc(310) (g), bcc(210) (h) of pure transition metal

surfaces. The atom below the top site for each surface facet is either the host atom (pure transition metal surfaces) or the single guest atom (single atom alloy metal surfaces).

Table S2. Primary features obtained from the literature.⁵ Electron affinity (EA in eV), ionization potential (IP in eV), and covalent radius (R) of the metal atom.

system	class	name	abbreviation
host	atomic	Electron affinity	EA*
		Ionization potential	IP*
		Atomic radius	R*
guest atom	atomic	Electron affinity	EA
		Ionization potential	IP
		Atomic radius	R

Table S3. Primary features obtained from DFT-RPBE calculations (spin-polarization effects are tested for and included where appropriate). Energy of the highest-occupied Kohn-Sham level (H in eV), energy of the lowest-unoccupied Kohn-Sham level (L in eV), binding energy of H with isolated metal atom (EH in eV as calculated by equation (2)), binding energy of metal dimers (EB in eV as calculated by equation (3)), binding distance of H with isolated metal atom (dH in Å), and binding distance of metal dimers of the metal atom; cohesive energy (EC in eV as calculated by equation (4)) and *d*-band center (DC in eV) of the bulk metal; *d*-band center of the top surface layer (DT in eV), *d*-band center of the subsurface layer (DS in eV), and the slab Fermi level (F in eV) of the metal surface.

system	class	name	abbreviation	
host	atomic	Energy of the highest-occupied Kohn-Sham level	H*	
		Energy of the lowest-unoccupied Kohn-Sham level	L*	
		Binding energy of H with single host metal atom	EH*	
		Binding energy of host metal dimers	EB*	
		Binding distance of H with single host metal atom	dH*	
		Binding distance of host metal dimer	dd*	
	bulk	Cohesive energy	EC*	
		<i>d</i> -band center	DC*	
		surface [#]	<i>d</i> -band center of the top surface layer	DT*
			<i>d</i> -band center of the subsurface layer	DS*
		Slab Fermi level	F*	
guest atom	atomic	Energy of the highest-occupied Kohn-Sham level	H	
		Energy of the lowest-unoccupied Kohn-Sham level	L	
		Binding energy of H with single guest metal atom	EH	
		Binding energy of guest metal dimers	EB	
		Binding distance of H with single guest metal atom	dH	

	Binding distance of guest metal dimers	dd
bulk	Cohesive energy	EC
	<i>d</i> -band center	DC

#the surface based primary features were calculated by using the unit cell consisting of one atom per atomic layer.

$$EH = E_{H\text{-metal}} - E_{\text{metal}} - E_H \quad (2)$$

where $E_{H\text{-metal}}$ is the energy of the total H-metal system, E_{metal} is the energy of the isolated metal atom, and E_H is the energy of the isolated H atom.

$$EB = E_{\text{metal-metal}} - 2E_{\text{metal}} \quad (3)$$

where $E_{\text{metal-metal}}$ is the energy of the total metal-metal dimer system, E_{metal} is the energy of the isolated metal atom.

$$EC = E_{\text{bulk}/n} - E_{\text{metal}} \quad (4)$$

where E_{bulk} is the energy of the bulk metal system, E_{metal} is the energy of the isolated metal atom, and n is the number of metal atoms in the bulk unit cell.

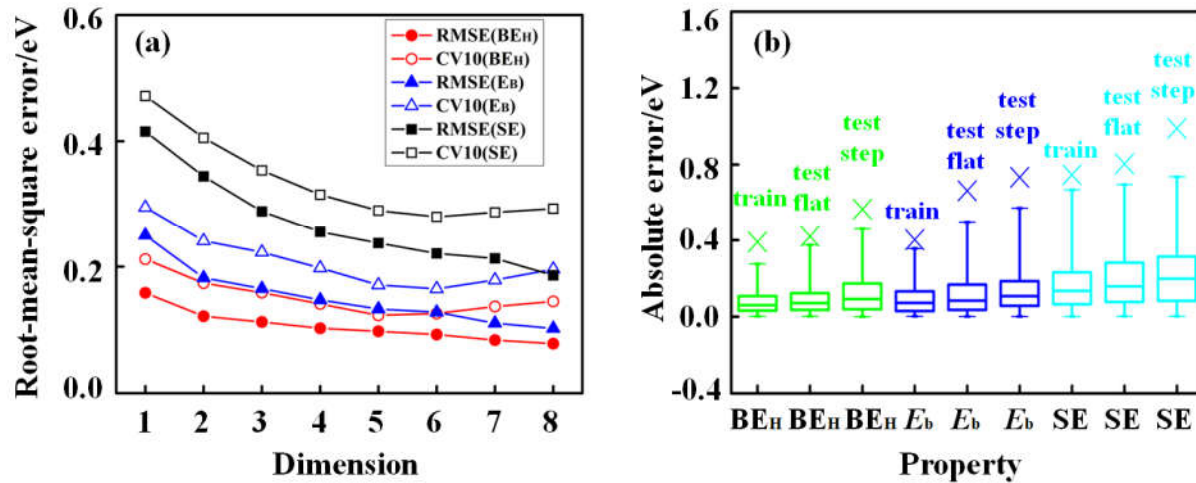


Figure S2. (a) RMSE and the averaged RMSE of the 10 fold cross-validation. (b) Box plots of the absolute errors for the training set and test set for the SISSO selected best models of BE_H (green), E_b (blue), and SE (cyan). The test set is divided into two parts: one part contains only flat surfaces and the other one contains only stepped surfaces. The upper and lower limits of the rectangles represent the 75th and 25th percentiles of the distribution, the internal horizontal lines mark the median (50th percentile), and the upper and lower limits of the error bars indicate the 99th and 1st percentiles. The crosses depict the maximum absolute errors.

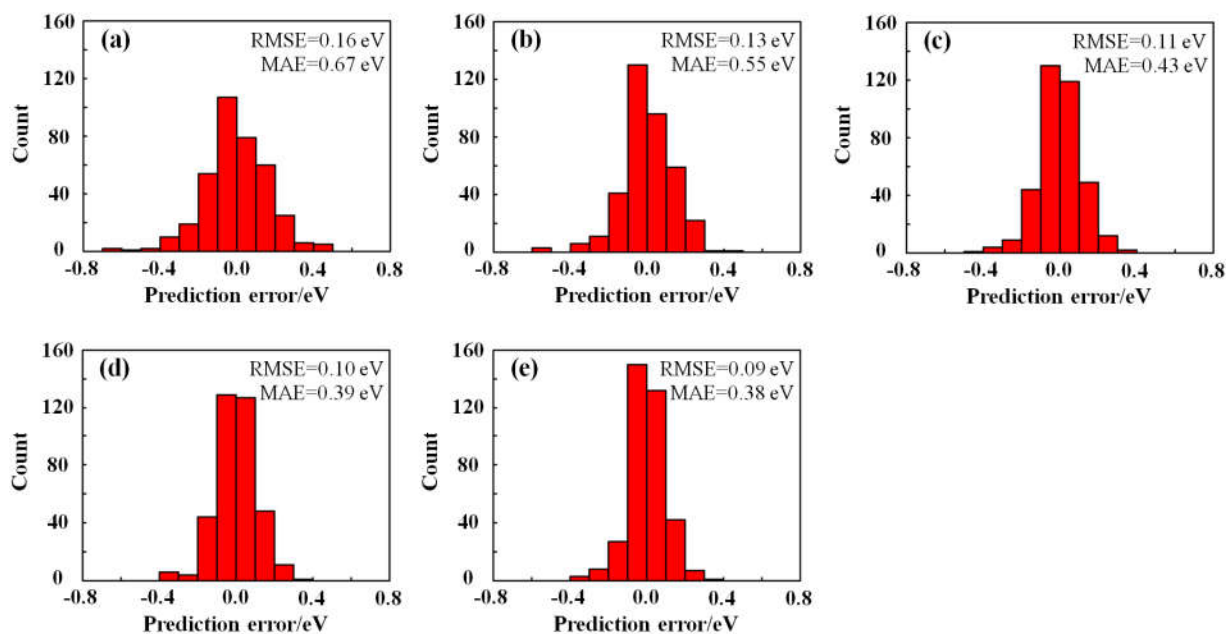


Figure S3. The error distributions for all the lower-dimensional models of BE_H : (a) 1D, (b) 2D, (c) 3D, and (d) 4D, and the SISSO selected best model (e) 5D.

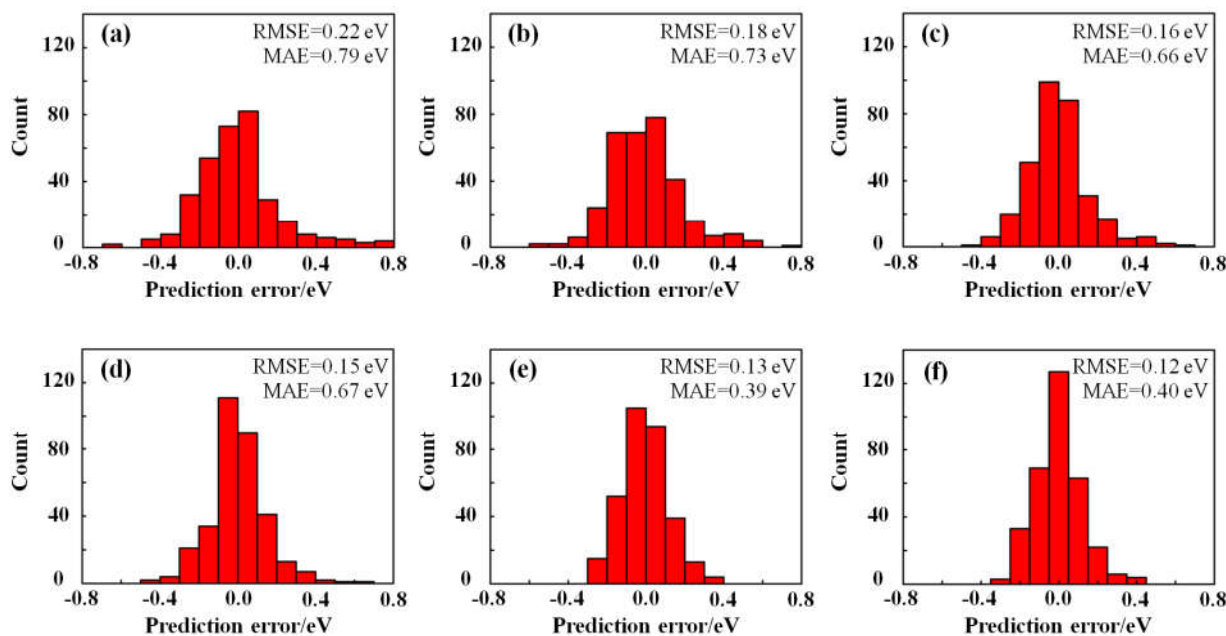


Figure S4. The error distributions for all the lower dimensional models of E_b : (a) 1D, (b) 2D, (c) 3D, (d) 4D, (e) 5D and the SISSO selected best model (f) 6D.

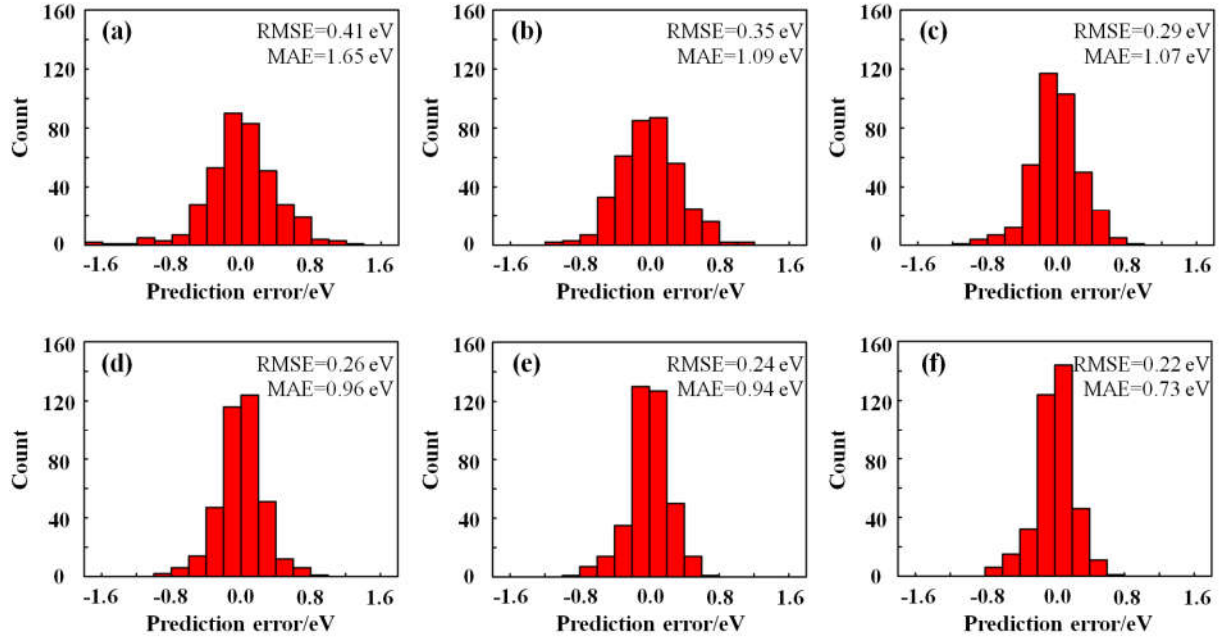


Figure S5. The error distributions for all the lower dimensional models of SE: (a) 1D, (b) 2D, (c) 3D, (d) 4D, (e) 5D and the SISSO selected best model (f) 6D.

Table S4. The top five largest deviations between calculated and predicted BE_H (in eV), E_b (in eV), and SE (in eV).

property	system	calculated	predicted	deviation
BE_H	Co/Ag(100)	-2.98	-2.60	0.38
	Co/Ag(110)	-2.98	-2.65	0.33
	Ni/Ti(0001)	-2.95	-3.27	0.33
	Ta/Ti(0001)	-3.19	-2.89	0.30
	Sc/Zn(0001)	-1.91	-2.21	0.30
E_b	Hf/Pt(111)	0.78	0.38	0.40
	Cu/Ag(110)	0.92	0.52	0.40
	Ir/Zr(0001)	0.68	0.28	0.40
	Pd/Ag(110)	0.60	0.24	0.36
	Zr/Cu(100)	0.71	0.38	0.33
SE	V/Pd(111)	-0.27	0.46	0.73
	Hg/Zn(0001)	-0.24	0.48	0.71
	Os/Zn(0001)	0.96	0.25	0.71
	Cd/Zn(0001)	-0.13	0.50	0.62
	Hg/Cd(0001)	-0.19	0.43	0.62

Table S5. Number of system with the predicted and calculated segregation energy meet the same condition of $SE < kT\ln(10)$ (N_{meet}), the total number of calculated systems (N_{total}), and the SE model's precision ($P = N_{\text{meet}}/ N_{\text{total}}$).

temperature	N_{meet}	N_{total}	P
200 K	345	360	95.83%
700 K	346	360	96.11%

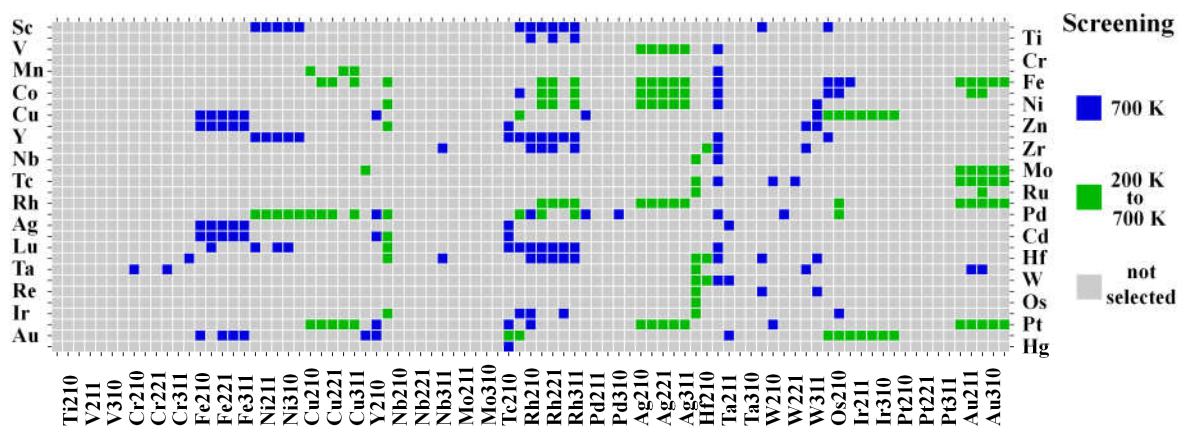
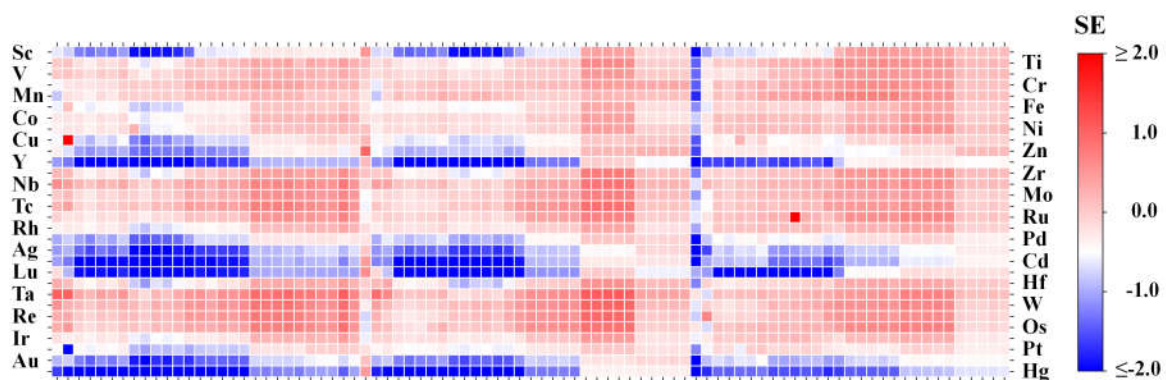
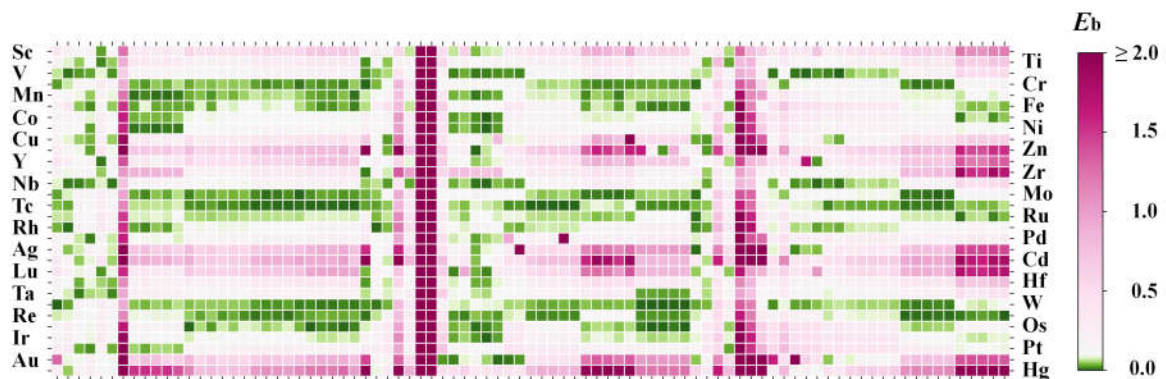
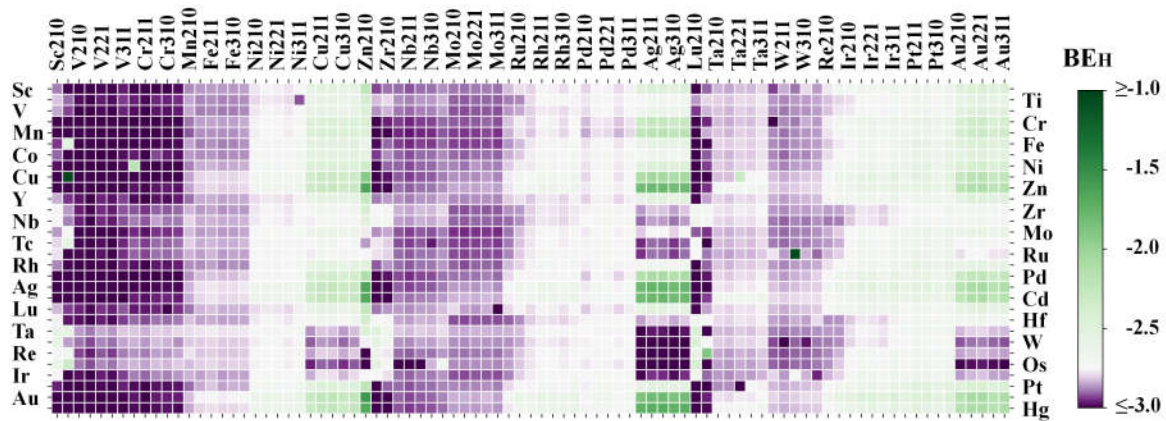


Figure S6. High-throughput screening of SAACs for (a) BE_H , (b) E_b , and (c) SE. The screened candidates are highlighted in (d). Vertical axis displays the guest atom type, and the vertical horizontal axis displays the host metal surfaces with different stepped surface cuts.

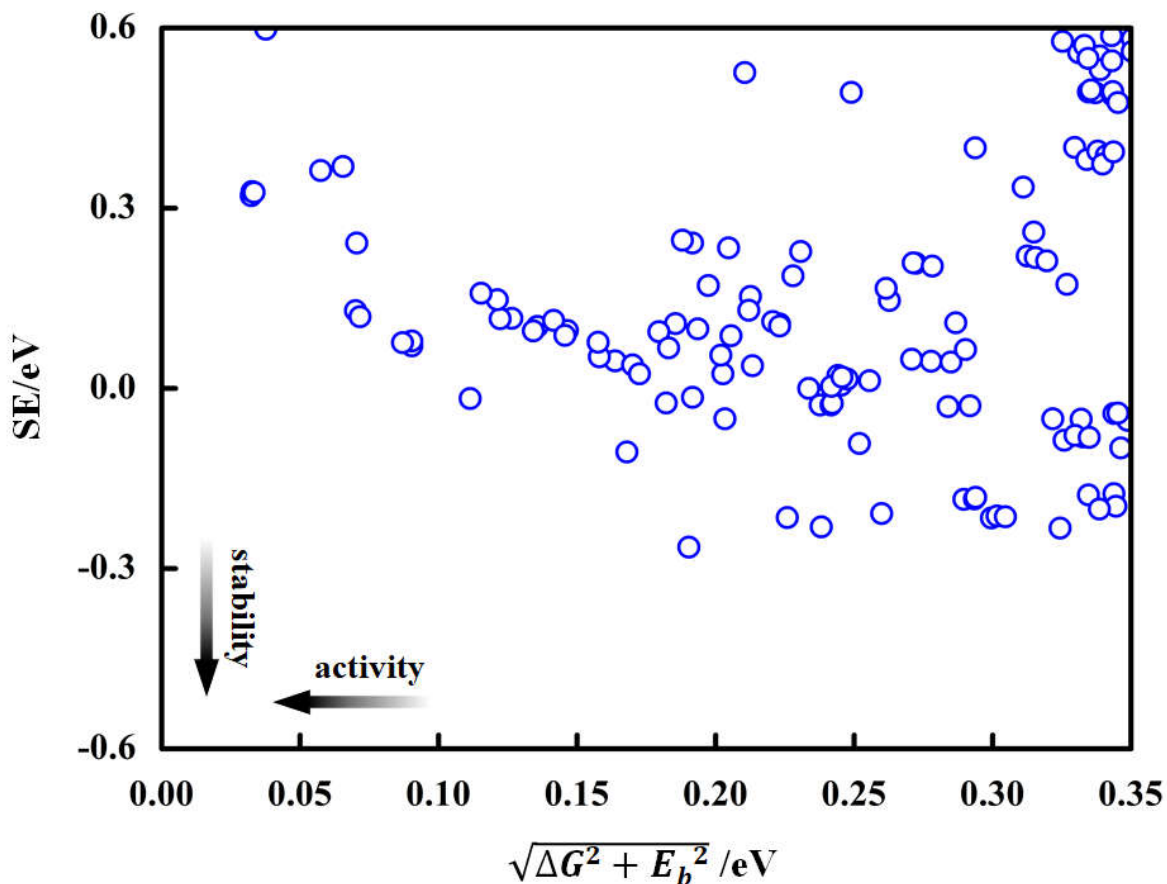


Figure S7. Stability vs. activity map for step SAACs surfaces at $T = 298 \text{ K}$ and $p = 1 \text{ atm}$. The SE on y-axis represents stability and activity parameter $\sqrt{\Delta G^2 + E_b^2}$ is shown on x-axis.

References

1. Hammer, B., Hansen, L.B. & Nørskov, J.K. Improved adsorption energetics within density-functional theory using revised Perdew-Burke-Ernzerhof functionals. *Physical Review B* **59**, 7413 (1999).
2. Blum, V. et al. Ab initio molecular simulations with numeric atom-centered orbitals. *Computer Physics Communications* **180**, 2175-2196 (2009).
3. Silbaugh, T.L. & Campbell, C.T. Energies of formation reactions measured for adsorbates on late transition metal surfaces. *The Journal of Physical Chemistry C* **120**, 25161-25172 (2016).
4. Henkelman, G., Uberuaga, B.P. & Jónsson, H. A climbing image nudged elastic band method for finding saddle points and minimum energy paths. *The Journal of Chemical*

- Physics* **113**, 9901-9904 (2000).
5. Dean, J.A. Lange's handbook of chemistry. (New york; London: McGraw-Hill, Inc., 1999).